HHS Public Access

Author manuscript

IEEE Trans Radiat Plasma Med Sci. Author manuscript; available in PMC 2023 May 01.

Published in final edited form as:

IEEE Trans Radiat Plasma Med Sci. 2022 May ; 6(5): 522–528. doi:10.1109/trpms.2021.3096534.

Performance of Dual-Ended Readout PET Detectors Based on BGO Arrays and $BaSO_4$ Reflector

Junwei Du [Senior Member, IEEE]

Department of Biomedical Engineering, University of California, Davis, CA 95616 USA

Abstract

In this paper, the performance of two dual-ended readout PET detectors based on 15 × 15 BGO arrays were compared. The crystal elements of one BGO array have polished lateral surfaces, while the crystal elements of the other BGO array have unpolished lateral surfaces. The two ends of the BGO elements are polished. The two BGO arrays both have a pitch size of 1.6 mm and thickness of 20 mm, and BaSO4 with a thickness of 80 μm was used as the reflector. Hamamatsu S14161-0305-08 SiPM arrays were used as photodetectors. All the measurements were performed at a bias voltage of 41.0 V and a temperature of 23.5 °C. The flood histograms show that all the crystal elements in the two BGO arrays were clearly resolved. The detector based on the BGO array with polished lateral surfaces provides an energy resolution of 16.9 ± 1.3%, timing resolution of 3.2 ± 0.2 ns, and DOI resolution of 18.4 ± 2.2 mm. In comparison, the detector based on the BGO array with unpolished lateral surfaces provides an energy resolution of 17.7 ± 2.0%, timing resolution of 3.5 ± 0.3 ns, and DOI resolution of 3.2 ± 0.2 mm.

Index Terms—

PET; DOI; BGO

I. Introduction

Small animal positron emission tomography (PET) has been widely used as a powerful tool for preclinical studies to image a wide range of biological processes in *vivo* since it was first developed in the 1990s [1]–[4]. Most of the currently available small animal PET scanners are based on lutetium oxyorthosilicate (LSO) or lutetium yttrium oxyorthosilicate (LYSO) [4]–[6], due to their high light yield, high stopping power, and fast decay time [7]. However, one of the drawbacks of lutetium-based crystals is the background radiation caused by ^{17}Lu, which limits small animal PET scanners for low-dose applications [8], [9]. Bismuth germanate (BGO), which has much lower background radiation, higher stopping power, and lower cost than these of lutetium-based crystals [10], is a promising candidate for building low-cost total-body small animal PET scanners with long axial field-of-view (FOV).

jwdu@ucdavis.edu .

Detectors with depth-of-interaction (DOI) information are essential to building small animal PET scanners with uniform resolution across the FOV [6], [11], [12]. Different DOI detector design methods have been proposed, such as multi-layer crystals [13], [14], crystal arrays with specially designed reflectors or crystal geometry [15]–[21], and dual-ended readout method [22]–[24]. Compared to other methods, the dual-ended readout detectors can provide better performance [25], [26]. Dual-ended readout detectors based on LYSO or LSO crystals have been well studied by optimizing the surface treatment, the reflector, and the coupling method between the reflector and the crystal [24], [27], [28]. However, until recently, dual-ended readout detectors based on BGO crystals and Toray reflector were investigated by ourselves using 8 × 8 BGO arrays with a pitch size of 2.2 mm coupled to SiPM arrays with the same pitch size [29]. Our results, replicated here briefly, showed that 1) dual-ended readout detectors based on polished BGO arrays and Toray reflector did not provide any DOI information. In contrast, polished LYSO arrays and Toray reflector do provide good DOI resolution, and 2) dual-ended readout detectors based on unpolished BGO arrays and Toray reflector provided good DOI information.

To further investigate and optimize BGO based dual-ended readout detectors, in this paper, the performance in term of flood histogram, energy resolution, timing resolution, and DOI resolution of two dual-ended readout detectors based on barium sulfate ($BaSO_4$) reflector and BGO arrays with polished and unpolished lateral surfaces were evaluated and compared. For the unpolished surfaces, after the crystals were cut using a saw, no more surfaces treatments were done.

II. Materials and Methods

A. Dual-ended readout detectors

Figure 1 shows the two 15 × 15 arrays of 1.52 × 1.52 × 20 mm^3 BGOs with polished lateral surfaces (Fig. 1 (left)) and unpolished lateral surfaces (Fig. 1 (right), which were named as polished BGO array and unpolished BGO array in this paper, respectively. The two ends of the BGO elements are polished. The two BGO arrays' pitch sizes are both 1.6 mm. $BaSO_4$ with a thickness of 80 μm was used as the inter-crystal reflector. The BGO material was grown by Shanghai Institute of Ceramics, Chinese Academy of Sciences (SICCAS), China, and the BGO arrays were fabricated by Sichuan Tianle Photonics Co., Ltd., China.

Two Hamamatsu SiPM arrays, S14161-0305-08s (Hamamatsu Photonics K.K., Japan), were used as photodetectors, which were coupled to both ends of the BGO arrays to construct the dual-ended readout detectors. Each S14161-0305-08 SiPM array has 8 × 8 SiPMs and a pitch size of 3.2 mm, and each SiPM pixel has an active area of 3.0 × 3.0 mm^2. The BGO arrays were coupled to the center of the SiPM arrays using optical grease BC-631 (Saint-Gobain S.A., France).

B. Readout electronics

The schematic of the readout electronics is shown in Fig. 2. Each detector module with two SiPM arrays has 128 SiPMs, and each SiPM has one anode and one cathode. To simplify the readout electronics, one common bias voltage was applied to the 128 anodes of SiPMs, and

the SiPM signals were extracted from the cathodes of SiPMs. For each SiPM array, the 64 SiPM signals were amplified individually and then summed according to row and column, generating 8 row-signals and 8 column-signals [30], [31]. A position encoding circuit was used to encoding the row and column signals, which reduces the 8 row-signals and 8 column-signals to 4 position signals (X^+, X^-, Y^+, and Y^-) [30], [31]. For one dual-ended readout detector with two SiPM arrays, it has 8 position signals and one timing signal. The timing signal is the sum of the 16 row-signals and the 16 column-signals of the two SiPM arrays.

The 8 position signals were digitized using a digitizer CAEN DT5740D (CAEN S.p.A., Italy) at a speed of 62.5 mega samples per second (MSPS). The timing signals of the dual-ended readout detector and the reference detector were both sent to constant fraction discriminators (CFDs, model 584, ORTEC, USA) for time pick-off, which were used as the start and stop signals of a time-to-amplitude converter (TAC, model 566, ORTEC, USA), respectively. The output of the TAC was also digitized by the digitizer DT5740D.

C. Experimental methods

All the experiments were performed using a ^{22}Na source with an active diameter of 0.25 mm and an activity of 50 μCi (model MMS06–022, Eckert & Ziegler Isotope Products, USA). The ^{22}Na was sealed in an epoxy capsule with a diameter of 25.4 mm and thickness of 6.1 mm. The dual-ended readout detector and the position encoding board were located in a light-tight enclosure, and the temperature inside the enclosure was maintained to be 23.5 ± 0.2 °C by blowing cool-dry air into the enclosure using an FTS XR AirJet Sample Cooler (model XR 401, SP Industries, Inc., USA). The temperature inside the enclosure was monitored using a thermocouple thermometer (model DIGI-SENSE WD-60010–10, Cole-Parmer Instrument Company, USA).

The bias voltage applied to the SiPM arrays was 41.0 V to obtain better flood histograms [31], and a 350–750 energy window was applied to each crystal to select events.

1) Flood histogram—The flood histogram data and the timing resolution data were acquired simultaneously using a reference detector consists of a polished LYSO cylinder with a diameter of 20 mm and thickness of 5 mm coupled to a Hamamatsu PMT R13349 (Hamamatsu Photonics K.K., Japan). The LYSO cylinder was wrapped with 6 layers of Teflon to maximum the light output. The distance between the reference detector and the ^{22}Na source was 3 cm, and the distance between the source and the dual-ended readout detector was 15 cm [32], [33]. For each measurement, 20 M events were acquired for further processing.

The gamma photon interaction positions (x, y) were calculated using the following formula:

$$x = \frac{\frac{X^+_{front} - X^-_{front}}{X^+_{front} + X^-_{front}} E^2_{front} + \frac{X^+_{rear} - X^-_{rear}}{X^+_{rear} + X^-_{rear}} E^2_{rear}}{E^2_{front} + E^2_{rear}}$$
$$y = \frac{\frac{Y^+_{front} - Y^-_{front}}{Y^+_{front} + Y^-_{front}} E^2_{front} + \frac{Y^+_{rear} - Y^-_{rear}}{Y^+_{rear} + Y^-_{rear}} E^2_{rear}}{E^2_{front} + E^2_{rear}} \quad (1)$$

$$E_{front} = X^+_{front} + X^-_{front} + Y^+_{front} + Y^-_{front}$$
$$E_{rear} = X^+_{rear} + X^-_{rear} + Y^+_{rear} + Y^-_{rear} \quad (2)$$

where X^+_{front}, X^-_{front} , Y^+_{front}, and Y^-_{front} were the four position signals of the SiPM array couple to the front end of the BGO array (closed to the ^{22}Na source), and X^+_{rear}, X^-_{rear} , Y^+_{rear} and Y^-_{rear} were the four position signals of the SiPM array coupled to the rear end of the BGO array (far from the ^{22}Na source). E_{front} and E_{rear} were the total energies detected by the two SiPM arrays coupled to the front and rear ends of the BGO array, respectively.

2) Energy resolution and 511 keV photopeak position—The energy resolution was calculated using the data obtained for the flood histograms. The energy spectrum was extracted for each crystal after using a crystal look-up table to assign events to each crystal. The center of a Gaussian fit to the 511 keV photopeak was used as the 511 keV photopeak position. The energy resolution was the ratio of the FWHM of the Gaussian fit to the 511 keV photopeak position. The average value and the standard deviation value of the energy resolution across the BGO array were used as a measure of the energy resolution of the detector.

3) Timing resolution—The timing resolution was also calculated for each crystal. The FWHM of a Gaussian fit to the timing spectrum was used as the timing resolution of that crystal. The average value and the standard deviation value of the timing resolution across the BGO array were used as a measure of the timing resolution of the detector. The timing resolution of two identical reference detectors was 200 ± 10 ps.

4) DOI resolution—The DOI resolution data were acquired at 9 depths (from 2 mm to 18 mm, with 2 mm intervals) using a reference detector consists of a Hamamatsu PMT R13349 coupled to a 0.5 × 20 ×20 mm^3 polished LYSO slab [22], [23]. The LYSO slab was wrapped with 5 layers of Teflon to maximum the light output. The distance between the reference detector and the ^{22}Na source, and the distance between the source and the dual-ended readout detector were both 10 cm (Fig.3 (top)). At each depth, 2 M events were acquired for further processing. The DOI information was calculated using

$$DOI = a\frac{E_{front} - E_{rear}}{E_{front} + E_{rear}} + b \quad (3)$$

where E_{front} and E_{rear} (equation 2) were the two energies detected by the two SiPM arrays coupled to the front end and rear end of the BGO array, respectively. Parameters 'a' and 'b' were the fit parameters used to model the DOI and the ratio of the two energies, respectively [29].

Due to the dual-ended readout detector was irradiated from one side using a reference detector (Fig.3 (top)) [33], only part of the crystals in the BGO array was irradiated and received sufficient counts for analysis, as shown in Fig. 3 (bottom). The 60 BGO crystals shown in the white rectangle were used as representatives to measure the DOI resolution of the detector, which was quantified as the FWHM of a Gaussian fit to the DOI distribution.

III. Results

A. Flood histogram

Figure 4 shows the flood histograms of the two detectors. All the crystal elements in the two BGO arrays were clearly resolved. The flood histogram qualities, which were calculated using the ratio of the distances to widths of the crystals spots [34], are 2.68 ± 0.24, and 2.65 ± 0.35 for detectors based on the polished BGO array (Fig. 4 (left)) and the unpolished BGO array (Fig. 4 (right)), respectively.

Figure 5 shows the position profiles of the 7^{th} crystal columns of the two BGO arrays, which were obtained from the flood histograms shown in Fig. 4. The peak-to-valley ratios of the position profiles were 6.3 ± 1.1 and 5.7 ± 1.2 for detectors based on the polished BGO array and the unpolished BGO array, respectively.

B. Energy resolution

The 511 keV photopeak position and the energy resolution for each crystal are shown in Figs. 6 and 7, respectively. The 511 keV photopeak position and the energy resolution of the edge BGO elements are worse than those of the center BGO elements, respectively, due to the scintillation photons escaping the edge crystals could not be collected by the SiPM arrays, which is a common phenomenon in PET detectors [17], [22].

The average 511 keV photopeak positions across the BGO arrays are 5530 ± 407 and 5392 ± 461 ADC channels for the detectors based on the polished BGO array and unpolished BGO array, respectively. The average energy resolutions are 16.9 ± 1.3% and 17.7 ± 2.0% for the detectors based on the polished BGO array and unpolished BGO array, respectively.

Figure 8 shows the 511 keV photopeak position and the energy resolution obtained at different depths, which were obtained using the data for the flood histogram. The 511 keV photopeak position of the detector based on the polished BGO array does not change with the DOI, while higher values of the 511 keV photopeak position were obtained at depths close to the two ends of the unpolished BGO array, which was caused by the loss of part of the scintillation photons to enhance DOI resolution before those scintillation photons reached the SiPM arrays [33]. The energy resolutions of both detectors obtained at different depths were similar (Fig. 8 (bottom)). The average energy resolutions across all depths and

crystals are 16.7 ± 1.3% and 16.8 ± 1.9% for the detectors based on the polished BGO array and the unpolished BGO array, respectively [33].

C. Timing resolution

Figure 9 shows the timing resolution for each crystal of the two BGO arrays. The average timing resolutions across the polished BGO array and the unpolished BGO array are 3.2 ± 0.2 ns and 3.5 ± 0.3 ns, respectively.

The average timing resolutions across all crystals obtained at different depths are shown in Fig. 10. The average timing resolutions of the detectors based on the polished BGO array does not change with DOI, while, slightly better timing resolutions were obtained at the two ends of the detector based on the unpolished BGO array, which corresponds to the 511 keV photopeak position shown in Fig. 8 (top). The average timing resolutions across all crystals and all depths for the detectors based on the polished BGO array and the unpolished BGO array are 3.2 ± 0.2 ns and 3.4 ± 0.2 ns, respectively [33].

D. DOI resolution

Figure 11 shows the DOI response for each crystal of the two detectors, and figure 12 shows the distribution of the DOI resolutions obtained for each crystal and at different depths. The average DOI resolutions across the 9 depths and the selected 60 crystals are 18.4 ± 2.2 mm and 3.2 ± 0.2 mm for the detectors based on the polished BGO array and the unpolished BGO array, respectively.

IV. Discussion and Conclusion

In this study, for the first time, the performances in terms of flood histogram, energy resolution, timing resolution, and DOI resolution of dual-ended readout detectors based on BGO arrays with different lateral surface treatments and $BaSO_4$ reflector were evaluated and compared. The flood histogram, energy resolution, and timing resolution of the polished BGO array are slightly better than these of the unpolished BGO array, however, the discrepancies are very small. However, a much better DOI resolution was obtained using the unpolished BGO array.

The flood histograms (Figs. 4 and 5) show that BGO arrays with a pitch size of 1.6 mm can be clearly resolved using SiPM arrays with a pitch size of 3.2 mm. The flood histograms also show that BGO arrays with smaller pitch sizes can be resolved. We will investigate the performance of detectors based on BGO arrays with a pitch size of ~1.0 mm for high-resolution small animal PET applications.

The energy resolutions are ~ 17 % for the two detectors. The energy resolution was not significantly affected by the DOI (Fig. 8 (bottom)). The obtained energy resolution is similar to these of dual-ended readout DOI encoding detectors based on LYSO/LSO arrays and Toray/ESR reflector [23], [31], but not as good as these of dual-ended readout DOI encoding detectors based on LYSO/LSO arrays and $BaSO_4$ reflector [35].

The timing resolutions of the two detectors were measured using a PMT based reference detector. The timing resolutions were also not significantly affected by the DOI (Fig. 10), which are ~3.2 ns and ~3.4 ns for detectors based on the polished BGO array and the unpolished BGO array, respectively. The estimated coincidence timing resolutions of two identical BGO arrays based detectors are ~ 5 ns, which is similar to other BGO based detectors with similar readout and crystal thicknesses [29], [36].

The DOI resolution of the detector based on the unpolished BGO array is 3.2 ± 0.2 mm, which is quite good and comparable to these of the dual-ended readout detectors based on polished LYSO arrays with a similar thickness [35], [37]. However, the DOI resolution of the detector based on the polished BGO array is 18.4 ± 2.2 mm, which is non-useful for 20 mm thick BGO arrays.

A signal multiplexing readout was used to reduce the 128 SiPM signals to 9 signals (8 for position information and 1 for timing information) to simplify the readout electronics. We anticipate that better performance, especially better flood histogram and timing resolution, can be obtained by reading out each SiPM individually [38]. However, the complexity and cost of the readout electronics will be significantly increased.

In conclusion, dual-ended readout detectors based on BGO arrays with unpolished lateral surfaces and $BaSO_4$ reflector can provide good flood histogram, energy resolution, timing resolution, and DOI resolution. They are good candidates for low-cost small-animal PET scanners and organ-dedicated scanners (such as brain PET scanners) aimed for low-activity studies [39], [40].

Acknowledgments

This work was supported by the National Institutes of Health under Grant R01 EB028806.

The author would like to thank Drs. Simon R. Cherry, Jinyi Qi, Qian Wang, and Chih-Chieh Liu from the University of California at Davis for useful discussions.

REFERENCES

[1]. Cherry SR et al. , “MicroPET: a high resolution PET scanner for imaging small animals,” IEEE Transactions on Nuclear Science, vol. 44, no. 3, pp. 1161–1166, Jun. 1997, doi: 10.1109/23.596981.

[2]. Chatziioannou AF, “Molecular imaging of small animals with dedicated PET tomographs,” Eur J Nucl Med, vol. 29, no. 1, pp. 98–114, Jan. 2002, doi: 10.1007/s00259-001-0683-3.

[3]. Myers R, “The biological application of small animal PET imaging,” Nuclear Medicine and Biology, vol. 28, no. 5, pp. 585–593, Jul. 2001, doi: 10.1016/S0969-8051(01)00213-X. [PubMed: 11516702]

[4]. Amirrashedi M, Zaidi H, and Ay MR, “Advances in Preclinical PET Instrumentation,” PET Clinics, vol. 15, no. 4, pp. 403–426, Oct. 2020, doi: 10.1016/j.cpet.2020.06.003. [PubMed: 32768368]

[5]. Miyaoka RS and Lehnert A, “Small animal PET: a review of what we have done and where we are going,” Phys. Med. Biol, 2020, doi: 10.1088/1361-6560/ab8f71.

[6]. Lai Y et al. , “H2RSPET: a 0.5 mm resolution high-sensitivity small-animal PET scanner, a simulation study,” Phys. Med. Biol, vol. 66, no. 6, p. 065016, Mar. 2021, doi: 10.1088/1361-6560/abe558. [PubMed: 33571980]

[7]. Du J, Wang Y, Zhang L, Zhou Z, Xu Z, and Wang X, “Physical Properties of LYSO Scintillator for NN-PET Detectors,” in 2009 2nd International Conference on Biomedical Engineering and Informatics, Oct. 2009, pp. 1–5. doi: 10.1109/BMEI.2009.5305107.

[8]. Bao Q and Chatziioannou AF, “Estimation of the minimum detectable activity of preclinical PET imaging systems with an analytical method,” Medical Physics, vol. 37, no. 11, pp. 6070–6083, 2010, doi: 10.1118/1.3495817. [PubMed: 21158319]

[9]. Freedenberg MI, Badawi RD, Tarantal AF, and Cherry SR, “Performance and limitations of positron emission tomography (PET) scanners for imaging very low activity sources,” Physica Medica, vol. 30, no. 1, pp. 104–110, Feb. 2014, doi: 10.1016/j.ejmp.2013.04.001. [PubMed: 23680361]

[10]. de Marcillac P, Coron N, Dambier G, Leblanc J, and Moalic J-P, “Experimental detection of α-particles from the radioactive decay of natural bismuth,” Nature, vol. 422, no. 6934, Art. no. 6934, Apr. 2003, doi: 10.1038/nature01541.

[11]. Yoshida E et al. , “Spatial resolution limits for the isotropic-3D PET detector X’tal cube,” Nuclear Instruments and Methods in Physics Research Section A: Accelerators, Spectrometers, Detectors and Associated Equipment, vol. 728, pp. 107–111, Nov. 2013, doi: 10.1016/j.nima.2013.06.104.

[12]. Shao Y, Sun X, Lan KA, Bircher C, Lou K, and Deng Z, “Development of a prototype PET scanner with depth-of-interaction measurement using solid-state photomultiplier arrays and parallel readout electronics,” Phys. Med. Biol, vol. 59, no. 5, pp. 1223–1238, Feb. 2014, doi: 10.1088/0031-9155/59/5/1223. [PubMed: 24556629]

[13]. Watanabe M et al. ., “Performance evaluation of a high-resolution brain PET scanner using four-layer MPPC DOI detectors,” Phys. Med. Biol, vol. 62, no. 17, pp. 7148–7166, Aug. 2017, doi: 10.1088/1361-6560/aa82e8. [PubMed: 28753133]

[14]. Akamatsu G et al. , “Performance evaluation of a whole-body prototype PET scanner with four-layer DOI detectors,” Phys. Med. Biol, vol. 64, no. 9, p. 095014, Apr. 2019, doi: 10.1088/1361-6560/ab18b2. [PubMed: 30978704]

[15]. Lee MS and Lee JS, “Depth-of-interaction measurement in a single-layer crystal array with a single-ended readout using digital silicon photomultiplier,” Phys. Med. Biol, vol. 60, no. 16, pp. 6495–6514, Aug. 2015, doi: 10.1088/0031-9155/60/16/6495. [PubMed: 26247294]

[16]. Berg E, Roncali E, Kapusta M, Du J, and Cherry SR, “A combined time-of-flight and depth-of-interaction detector for total-body positron emission tomography,” Medical Physics, vol. 43, no. 2, pp. 939–950, 2016, doi: 10.1118/1.4940355. [PubMed: 26843254]

[17]. Pizzichemi M et al. , “On light sharing TOF-PET modules with depth of interaction and 157 ps FWHM coincidence time resolution,” Phys. Med. Biol, vol. 64, no. 15, p. 155008, Aug. 2019, doi: 10.1088/1361-6560/ab2cb0. [PubMed: 31239430]

[18]. LaBella A, Zhao W, Lubinsky R, and Goldan AH, “Prismatoid light guide array for enhanced gamma ray localization in PET: a Monte Carlo simulation study of scintillation photon transport,” Phys. Med. Biol, vol. 65, no. 18, p. 18LT01, Sep. 2020, doi: 10.1088/1361-6560/ab9373.

[19]. Valenciaga Y, Prout DL, Taschereau R, and Chatziioannou AF, “Feasibility of Using Crystal Geometry for a DOI Scintillation Detector,” IEEE Transactions on Radiation and Plasma Medical Sciences, vol. 2, no. 3, pp. 161–169, May 2018, doi: 10.1109/TRPMS.2017.2760857. [PubMed: 31098432]

[20]. Yoshida E, Obata F, Kamada K, and Yamaya T, “Development of Single-Ended Readout DOI Detector With Quadrisected Crystals,” IEEE Transactions on Radiation and Plasma Medical Sciences, vol. 4, no. 5, pp. 563–569, Sep. 2020, doi: 10.1109/TRPMS.2020.2990788.

[21]. Yoshida E, Obata F, Kamada K, and Yamaya T, “A crosshair light sharing PET detector with DOI and TOF capabilities using four-to-one coupling and single-ended readout,” IEEE Transactions on Radiation and Plasma Medical Sciences, pp. 1–1, 2020, doi: 10.1109/TRPMS.2020.3032466.

[22]. Du J et al. , “Performance of a high-resolution depth-encoding PET detector module using linearly-graded SiPM arrays,” Phys. Med. Biol, vol. 63, no. 3, p. 035035, Feb. 2018, doi: 10.1088/1361-6560/aaa707. [PubMed: 29324437]

[23]. Yang Q, Kuang Z, Sang Z, Yang Y, and Du J, “Performance comparison of two signal multiplexing readouts for SiPM-based pet detector,” Phys. Med. Biol, vol. 64, no. 23, p. 23NT02, Dec. 2019, doi: 10.1088/1361-6560/ab5738.

[24]. Kang HG et al. , “Crystal surface and reflector optimization for the SiPM-based dual-ended readout TOF-DOI PET detector,” Biomed. Phys. Eng. Express, 2020, doi: 10.1088/2057-1976/abc45a.

[25]. Ito M, Hong SJ, and Lee JS, “Positron emission tomography (PET) detectors with depth-of-interaction (DOI) capability,” Biomed. Eng. Lett, vol. 1, no. 2, p. 70, Jun. 2011, doi: 10.1007/s13534-011-0019-6.

[26]. Mohammadi I, Castro IFC, Correia PMM, Silva ALM, and Veloso JFCA, “Minimization of parallax error in positron emission tomography using depth of interaction capable detectors: methods and apparatus,” Biomed. Phys. Eng. Express, vol. 5, no. 6, p. 062001, Oct. 2019, doi: 10.1088/2057-1976/ab4a1b.

[27]. Ren S, Yang Y, and Cherry SR, “Effects of reflector and crystal surface on the performance of a depth-encoding PET detector with dual-ended readout,” Medical Physics, vol. 41, no. 7, p. 072503, 2014, doi: 10.1118/1.4881097. [PubMed: 24989406]

[28]. Kuang Z et al. , “Dual-ended readout small animal PET detector by using 0.5 mm pixelated LYSO crystal arrays and SiPMs,” Nuclear Instruments and Methods in Physics Research Section A: Accelerators, Spectrometers, Detectors and Associated Equipment, vol. 917, pp. 1–8, Feb. 2019, doi: 10.1016/j.nima.2018.11.011.

[29]. Du J, Ariño-Estrada G, Bai X, and Cherry SR, “Performance comparison of dual-ended readout depth-encoding PET detectors based on BGO and LYSO crystals,” Phys. Med. Biol, vol. 65, no. 23, p. 235030, Nov. 2020, doi: 10.1088/1361-6560/abc365.

[30]. Popov V, Majewski S, and Weisenberger AG, “Readout electronics for multianode photomultiplier tubes with pad matrix anode layout,” in 2003 IEEE Nuclear Science Symposium. Conference Record (IEEE Cat. No.03CH37515), Oct. 2003, vol. 3, pp. 2156–2159 Vol.3. doi: 10.1109/NSSMIC.2003.1352307.

[31]. Du J, Bai X, and Cherry SR, “Performance comparison of depth-encoding detectors based on dual-ended readout and different SiPMs for high-resolution PET applications,” Phys. Med. Biol, vol. 64, no. 15, p. 15NT03, Aug. 2019, doi: 10.1088/1361-6560/ab1c37.

[32]. Du J, Bai X, and Cherry SR, “A depth-of-interaction encoding PET detector module with dual-ended readout using large-area silicon photomultiplier arrays,” Phys. Med. Biol, vol. 63, no. 24, p. 245019, Dec. 2018, doi: 10.1088/1361-6560/aaee32. [PubMed: 30523925]

[33]. Du J, Bai X, Liu C-C, Qi J, and Cherry SR, “Design and evaluation of gapless curved scintillator arrays for simultaneous high-resolution and high-sensitivity brain PET,” Phys. Med. Biol, vol. 64, no. 23, p. 235004, Nov. 2019, doi: 10.1088/1361-6560/ab4e3c. [PubMed: 31618708]

[34]. Du J et al. , “Characterization of Large-Area SiPM Array for PET Applications,” IEEE Transactions on Nuclear Science, vol. 63, no. 1, pp. 8–16, Feb. 2016, doi: 10.1109/TNS.2015.2499726. [PubMed: 27182077]

[35]. Yang Q, Wang X, Kuang Z, Zhang C, Yang Y, and Du J, “Evaluation of Two SiPM Arrays for Depth-Encoding PET Detectors Based on Dual-Ended Readout,” IEEE Transactions on Radiation and Plasma Medical Sciences, pp. 1–1, 2020, doi: 10.1109/TRPMS.2020.3008710.

[36]. Zhang H et al. , “Performance Characteristics of BGO Detectors for a Low Cost Preclinical PET Scanner,” IEEE Transactions on Nuclear Science, vol. 57, no. 3, pp. 1038–1044, Jun. 2010, doi: 10.1109/TNS.2010.2046753. [PubMed: 21165154]

[37]. Li M, Wang Y, and Abbaszadeh S, “Development and initial characterization of a high-resolution PET detector module with DOI,” Biomed. Phys. Eng. Express, vol. 6, no. 6, p. 065020, Nov. 2020, doi: 10.1088/2057-1976/abbd4f.

[38]. Aguilar A et al. , “Timing Results Using an FPGA-Based TDC with Large Arrays of 144 SiPMs,” IEEE Transactions on Nuclear Science, vol. 62, no. 1, pp. 12–18, Feb. 2015, doi: 10.1109/TNS.2014.2359078.

[39]. Ouyang Y, Kim TJ, and Pratx G, “Evaluation of a BGO-Based PET System for Single-Cell Tracking Performance by Simulation and Phantom Studies,” Mol Imaging, vol. 15, p. 1536012116646489, Jan. 2016, doi: 10.1177/1536012116646489.

[40]. van Dongen GAMS, Boellaard R, and Vugts DJ, “In vivo tracking of single cells with PET,” Nature Biomedical Engineering, vol. 4, no. 8, Art. no. 8, Aug. 2020, doi: 10.1038/s41551-020-0598-6.

Fig. 1.
Photographs of (left) the polished BGO array and (right) the unpolished BGO array.

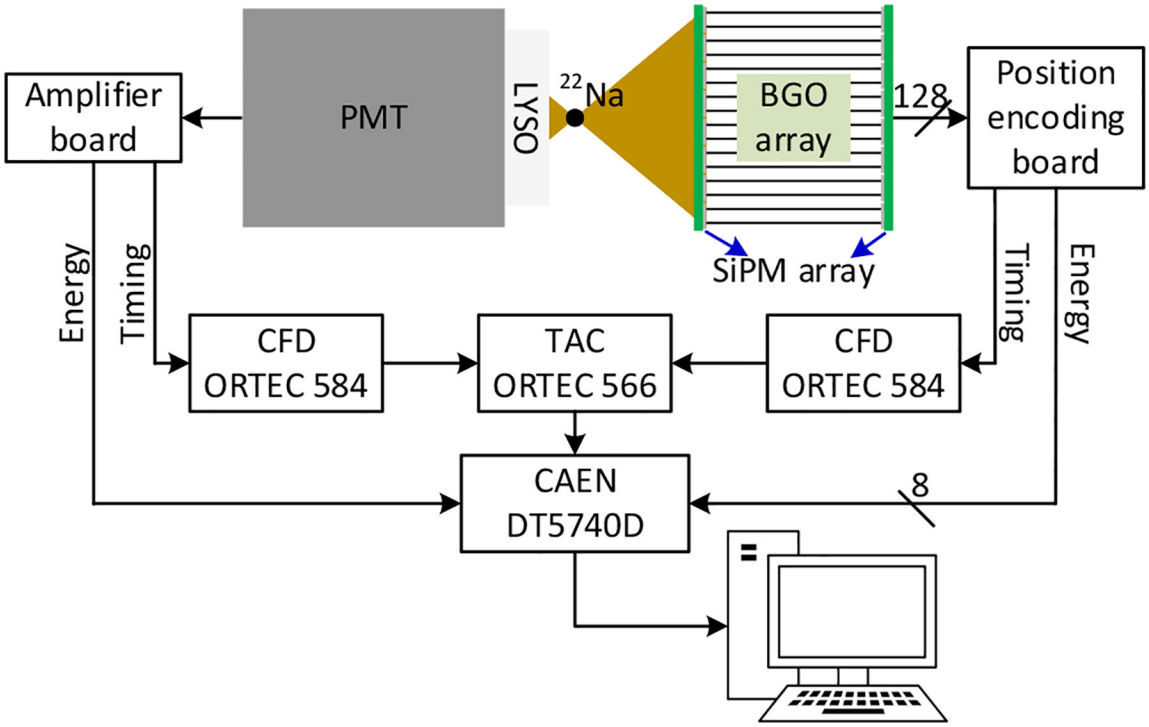

Fig. 2.

Schematic of the readout electronics for flood histogram and timing measurements. During the DOI resolution measurement, the dual-ended readout detector was irradiated from one side using a reference detector based on Hamamatsu PMT R13349 and a 0.5 × 20 × 20 mm^3 LYSO slab (Fig. 3 (top)).

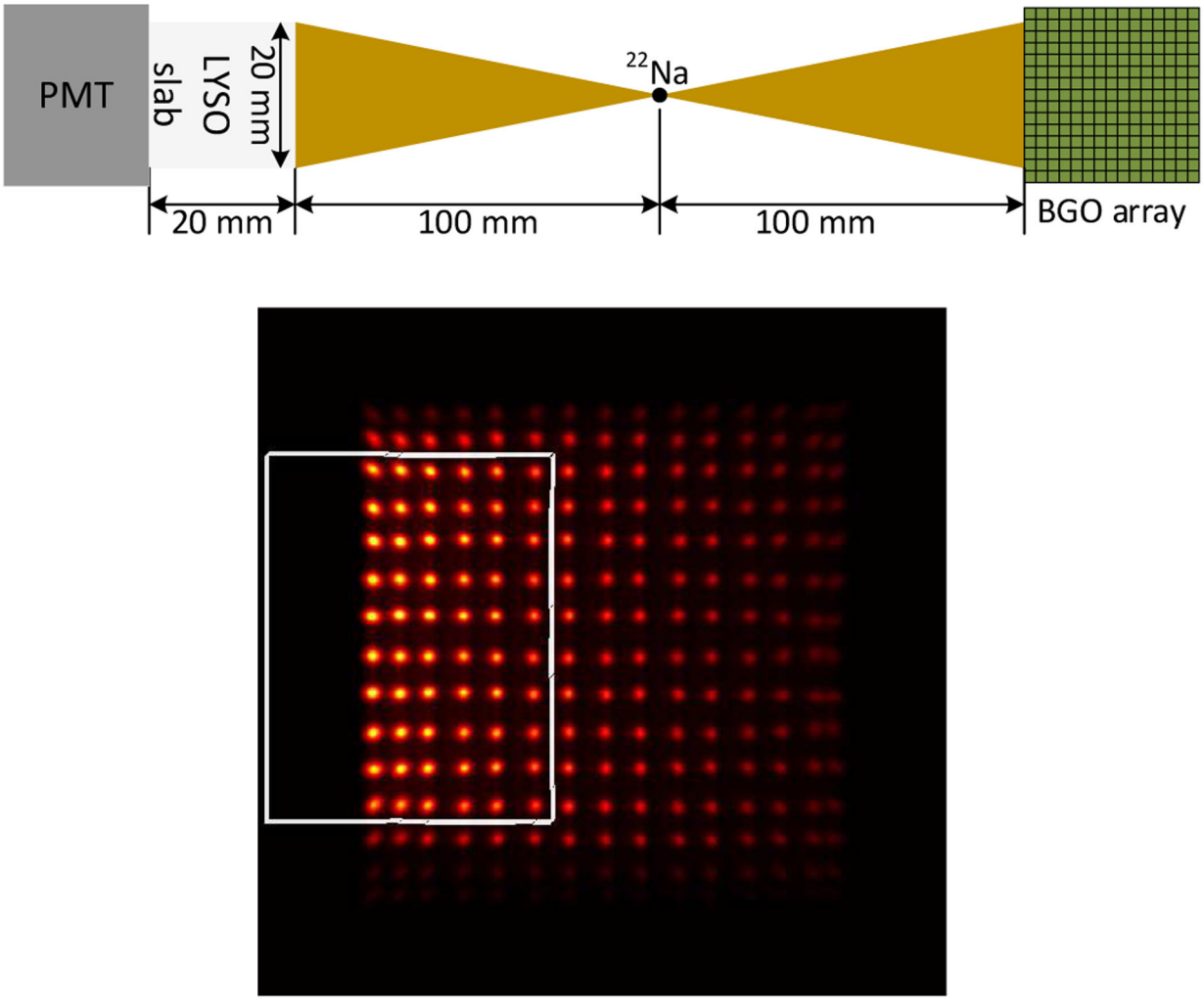

Fig. 3.
(top) diagram of the DOI setup, and (bottom) flood histogram obtained during DOI resolution measurements. The 6 × 10 crystals in the white rectangle were used as representative crystals to measure the DOI resolution of the detector.

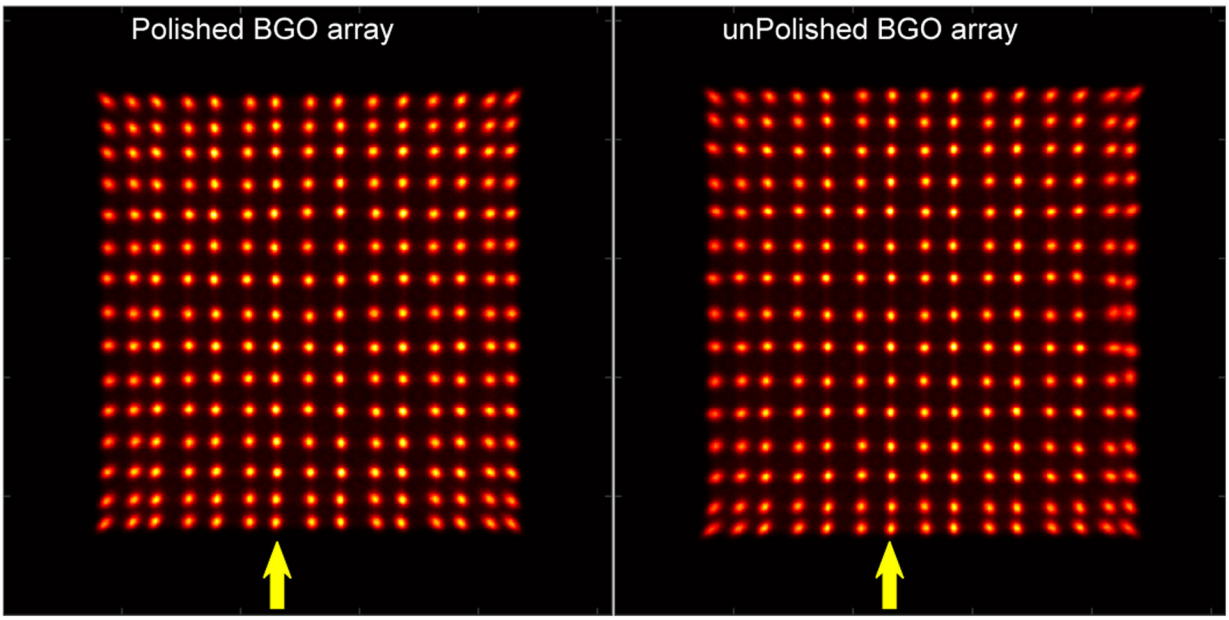

Fig. 4.

Flood histograms of the detectors based on (left) the polished BGO array and (right) the unpolished BGO array. The yellow arrows indicate the 7th crystal columns used in Fig. 5.

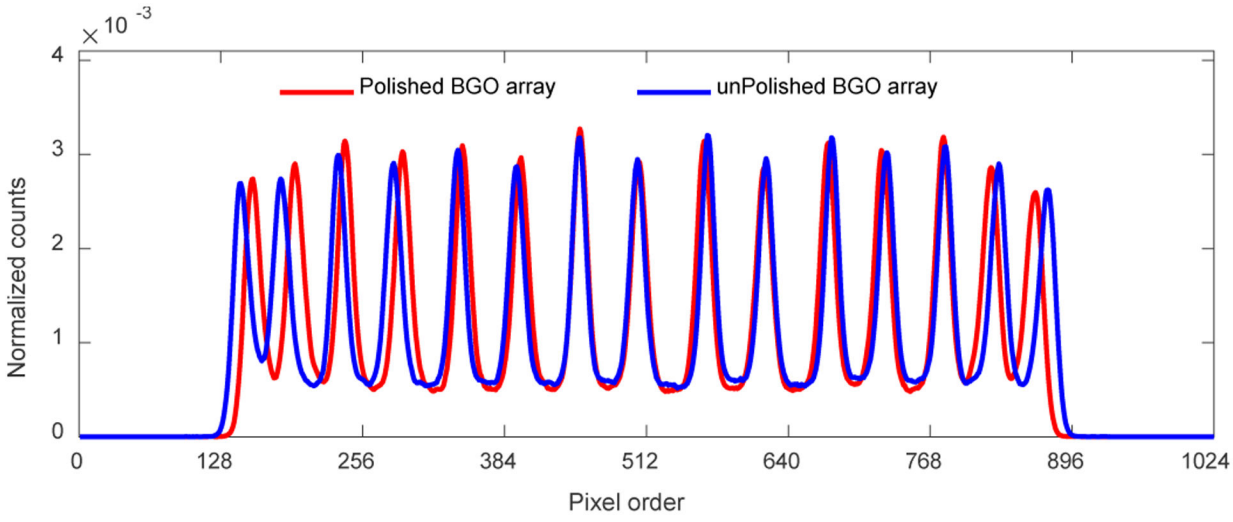

Fig. 5.

Position profiles of the 7th crystal column, which were obtained from the flood histogram shown in Fig. 4. The 7th crystal columns were registered from left as indicated by the yellow arrows in Fig.4

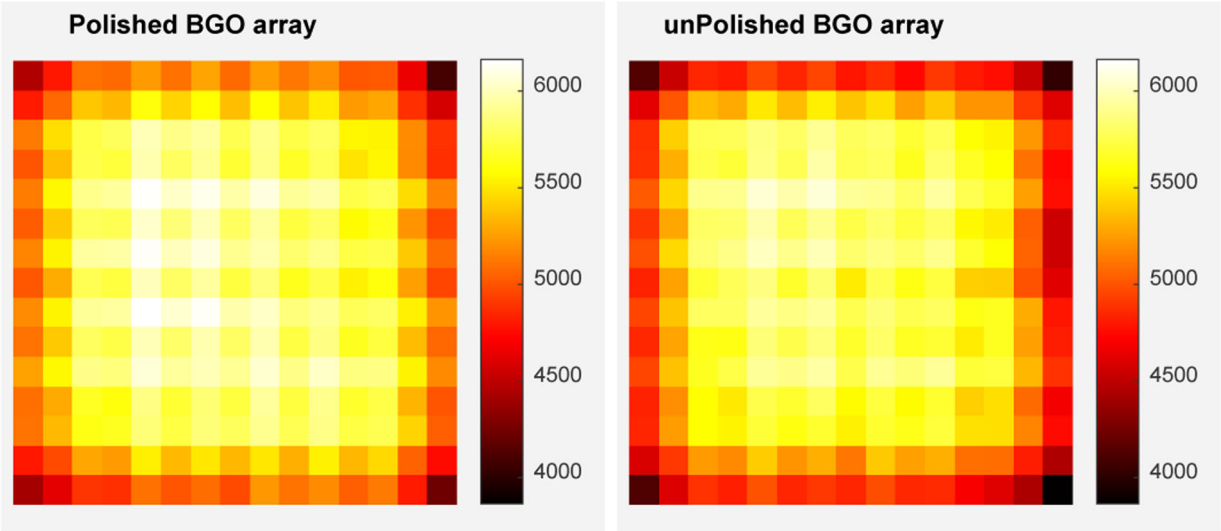

Fig. 6.

The 511 keV photopeak position for each crystal of (left) the polished BGO array and (right) the unpolished BGO array. The units of the color bars are in ADC channels.

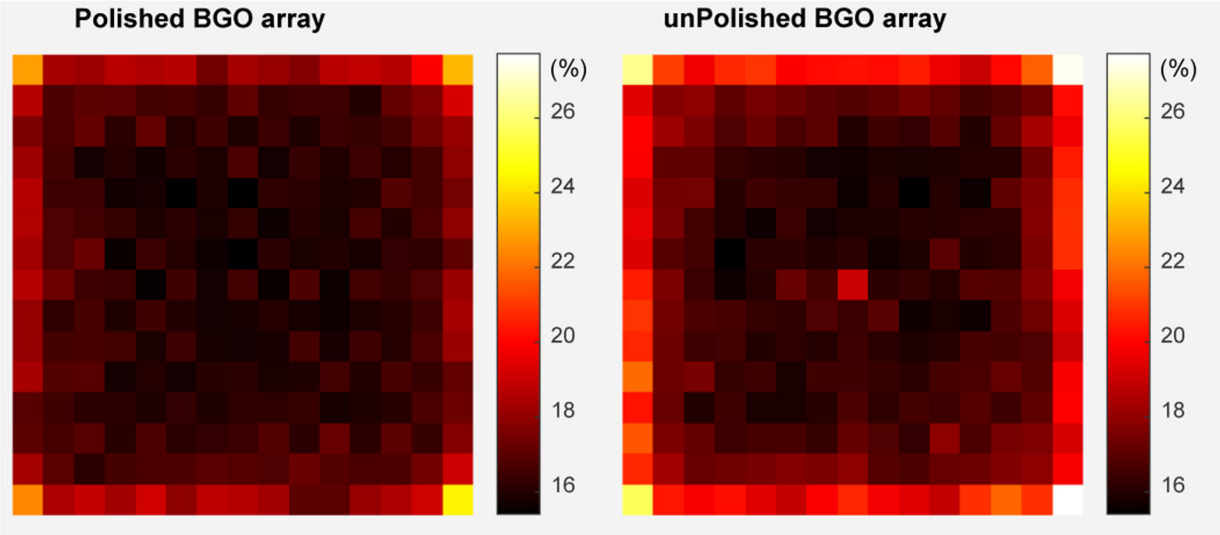

Fig. 7.
The energy resolution for each crystal of (left) the polished BGO array and (right) the unpolished BGO array.

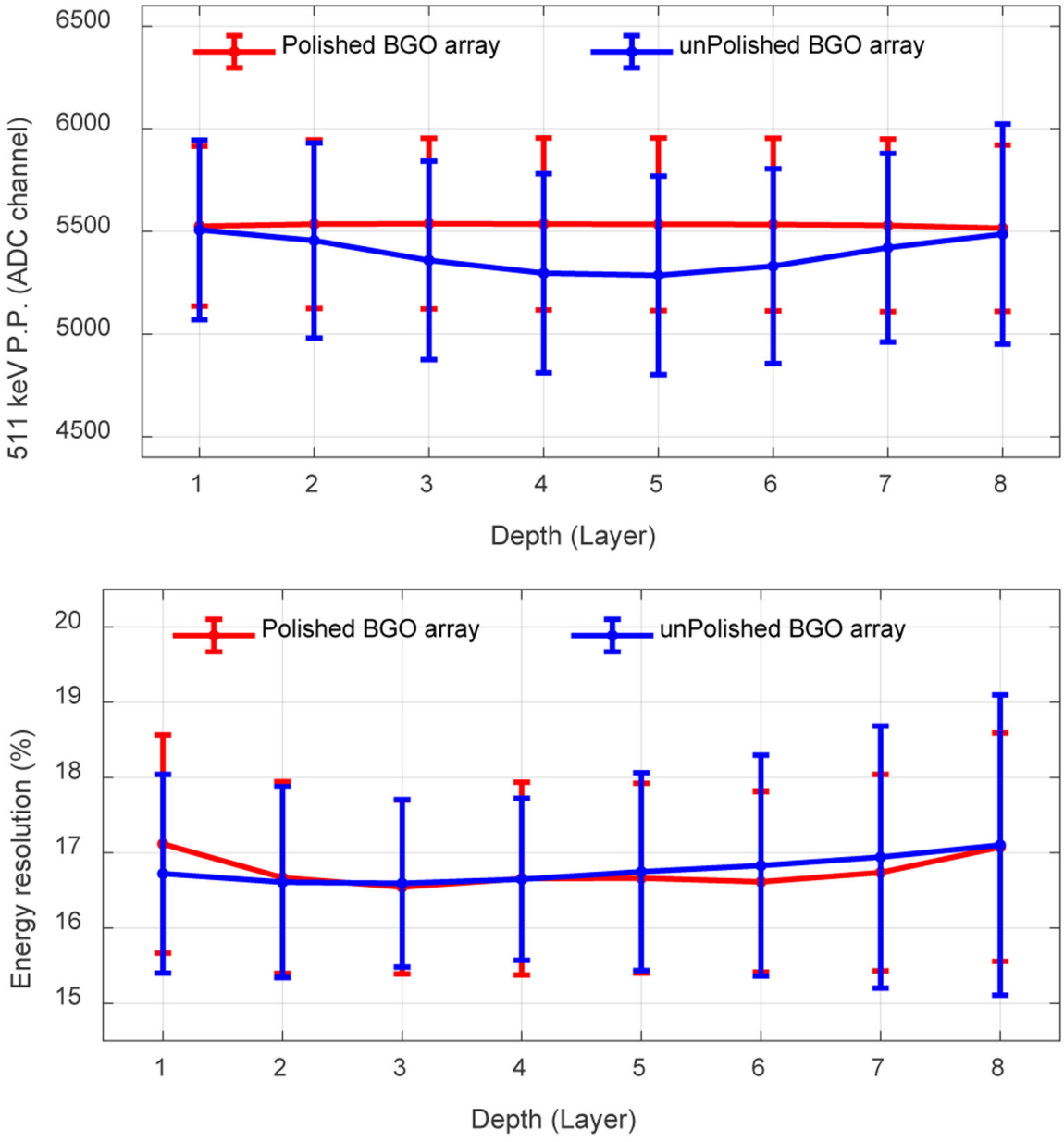

Fig. 8.

(top) The average 511 keV photopeak position and (bottom) the average energy resolution versus depth. Each layer has a thickness of 2.5 mm. The error bars are the standard deviation of the 511 keV photopeak position (P.P.) (top figure) or the energy resolution (bottom figure) across all crystals. Data for flood histogram was used.

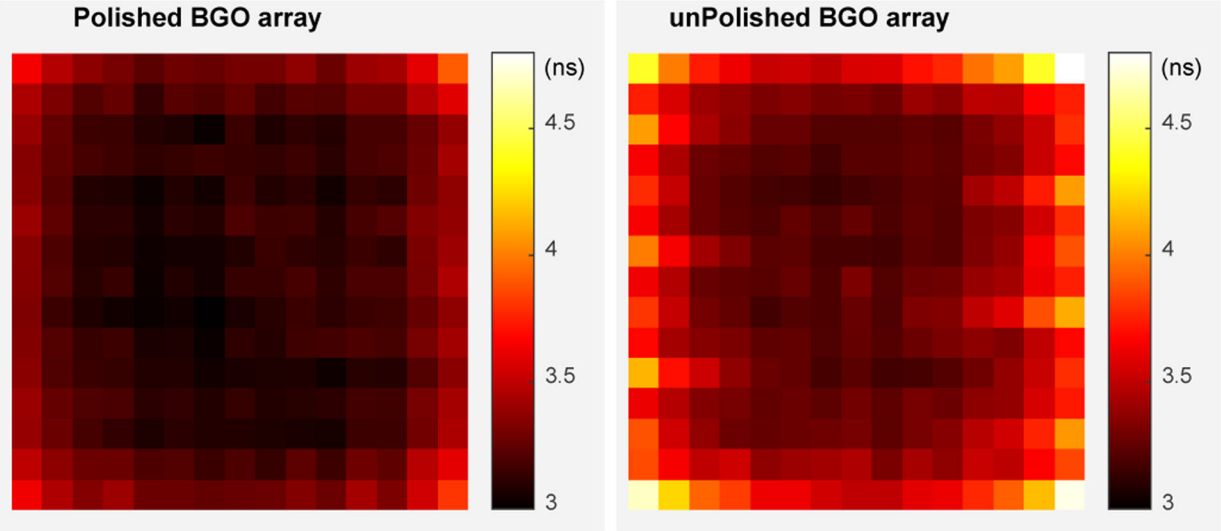

Fig. 9.
Timing resolutions for each crystal of (left) the polished BGO array and (right) the unpolished BGO array.

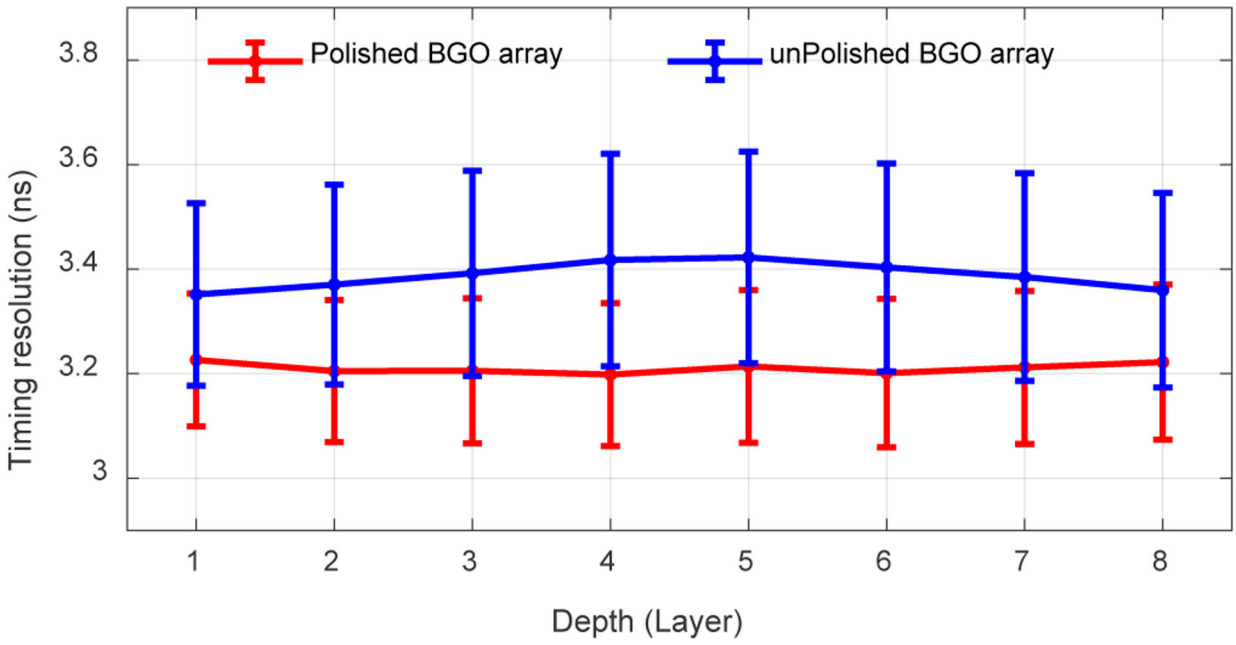

Fig. 10.

Average timing resolutions versus depth. The error bars are the standard deviation values of the timing resolution across the BGO arrays. Data for flood histogram was used.

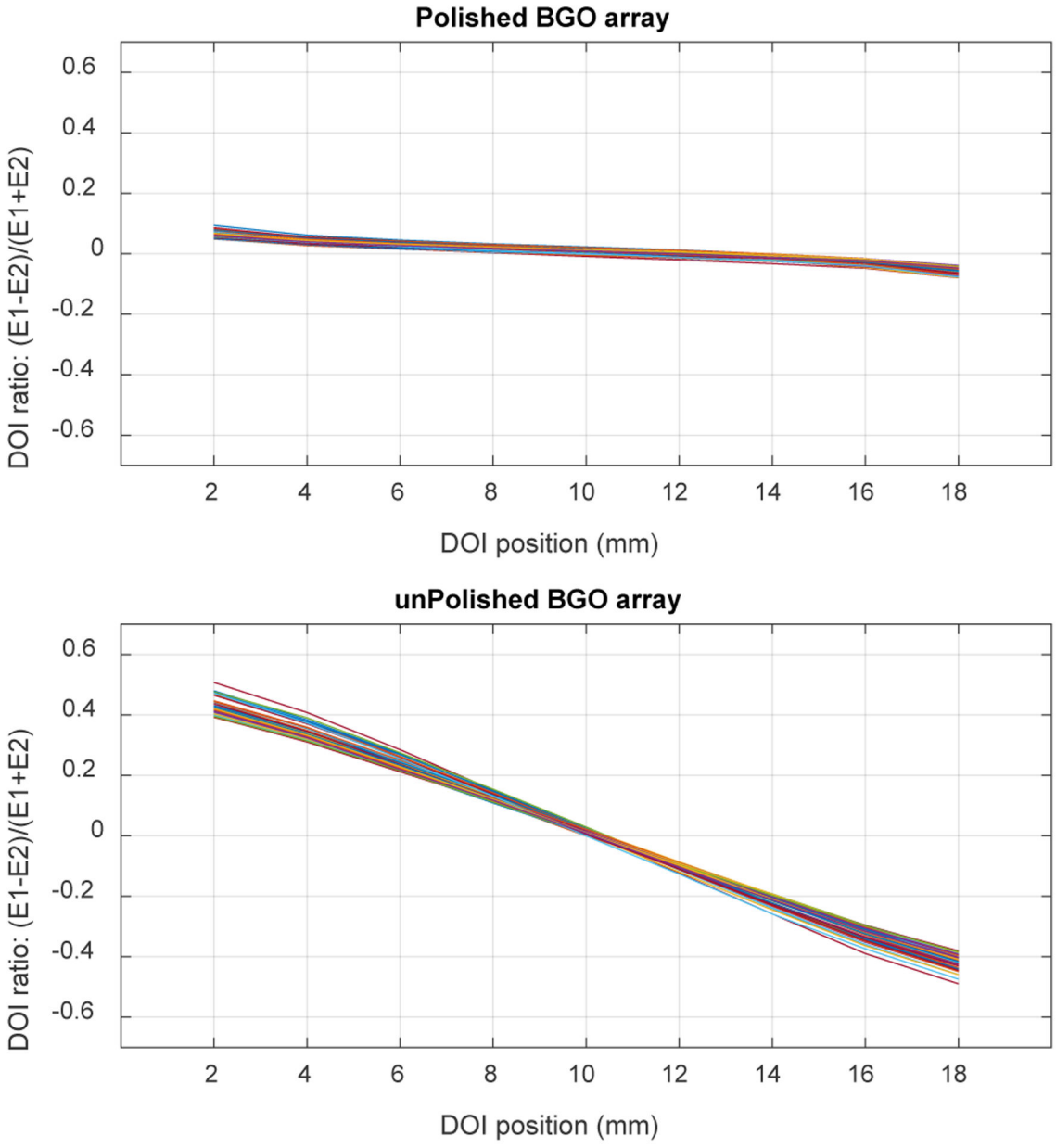

Fig. 11.

DOI response for each of the selected crystals of (top) the polished BGO array and (bottom) the unpolished BGO array.

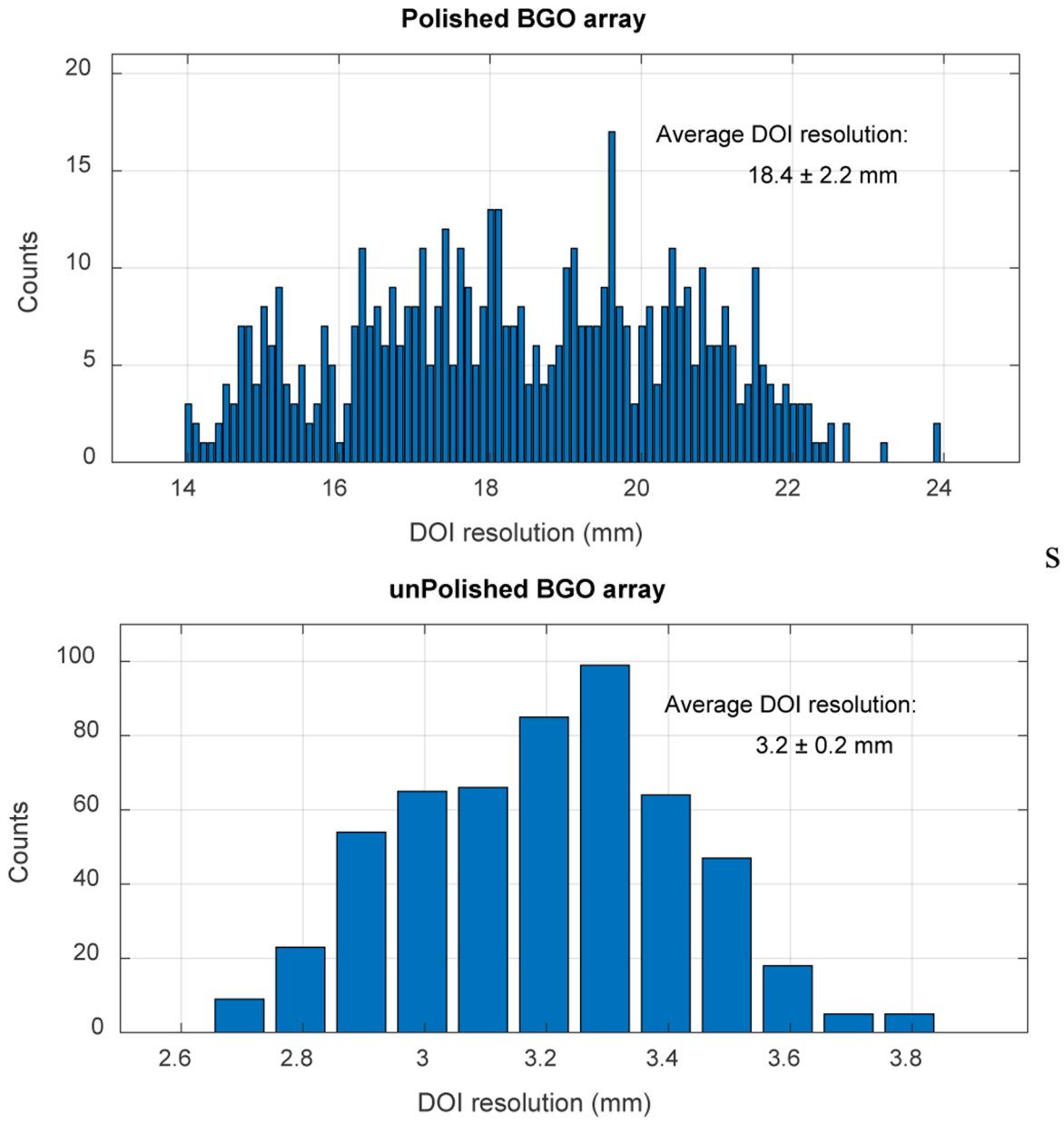

S

Fig. 12.

Distribution of the DOI resolution across the selected 60 crystals and the 9 depths of (top) the polished BGO array and (bottom) the unpolished BGO array.